

# Emerging Quadrature Lattices of Kerr Combs

Eran Lustig<sup>1\*†</sup>, Melissa A. Guidry<sup>1†</sup>, Daniil M. Lukin<sup>1</sup>,  
Shanhui Fan<sup>1</sup>, Jelena Vučković<sup>1</sup>

<sup>1</sup>Edward L. Ginzton Laboratory, Stanford University, Stanford, 94305,  
CA, USA.

\*Corresponding author(s). E-mail(s): [elustig@stanford.edu](mailto:elustig@stanford.edu);

†These authors contributed equally to this work.

## Abstract

A quadrature lattice is a coupled array of field quadratures that offers new avenues in shaping the quantum properties of multimode light [1–3]. Such lattices are described within the framework of non-Hermitian, non-dissipative physics and exhibit intriguing lattice phenomena such as lattice exceptional points, edge-states, entanglement and non-Hermitian skin effect, offering fundamentally new methods for controlling quantum fluctuations [1, 4]. Nonlinear resonators are suitable for studying multimode pair-generation processes and squeezing which are non-dissipative in  $\chi^{(2)}$  and  $\chi^{(3)}$  materials [5–12], but observing non-Hermitian lattice phenomena in photonic quadrature lattices was not achieved. Remarkably, in dissipative Kerr microcombs [13], which have revolutionized photonic technology, such lattices emerge and govern the quantum noise that leads to comb formation. Thus, they offer a unique opportunity to realize quadrature lattices, and to study and manipulate multimode quantum noise which is essential for any quantum technology. Here, we experimentally study non-Hermitian lattice effects in photonic quadrature lattices for the first time. Our photonic quadrature lattices emerge at Kerr microcomb transitions, allowing us to observe fundamental connections between dispersion symmetry, frequency-dependent squeezed supermodes, and non-Hermitian lattice physics in an integrated setup. Our work unifies two major fields, quantum non-Hermitian physics and Kerr combs, and opens the door to utilizing dissipative Kerr combs to experimentally explore rich non-Hermitian physics in the quantum regime, engineer quantum light, and develop new tools to study the quantum noise and formation of Kerr combs.

# 1 Introduction

In recent years, there has been growing interest in photonic quadrature lattices and their quantum properties [1]. Unlike conventional photonic lattices, where the lattice sites are coherent field amplitudes, in photonic quadrature lattices, each discrete site consists of two optical quadratures that are coupled to other quadratures. Since the quadrature representation forms the natural basis for continuous variable (CV) [14] quantum states, photonic quadrature lattices enable the understanding of rich multimode systems from the perspective of squeezing and deterministic entanglement generation. Notably, Hermitian quadratic bosonic lattices translate to non-Hermitian lattices in quadrature space. Thus, the rich physics of non-Hermitian lattices, which includes a plethora of effects such as optical exceptional points [15], the non-Hermitian skin effect [16], and beyond, manifests in quadrature space with novel implications for squeezing and entanglement [2, 4, 16, 17].

In contrast to traditional non-Hermitian optical lattices, where the interplay between gain and loss is governed by photon absorption, quadrature lattice dynamics are governed by parametric processes (*i.e.*, energy-conserving) such as nonlinear optical pair creation and annihilation. Thus, the realization of a bosonic quadrature lattice requires both multimode parametric gain and loss, and the coupling or transfer of bosons between lattice sites. In recent experiments, non-Hermitian lattice effects in quadrature lattices were observed in optomechanics in the synthetic dimension [2, 3, 18] by coupling several parametrically pumped opto-mechanical resonator modes together. In photonics, a fruitful approach for observing non-Hermitian lattice physics is along the synthetic frequency dimension of a single optical cavity, in which the optical modes are coupled by modulation at the free spectral range (FSR) frequency [19–21]. Such lattices can also be realized in a nonlinear environment [22], and even in the non-dissipative quantum regime by coupling photons generated across multiple frequency modes by second-order pair production with electro-optic modulation [8]. However, observing quadrature lattices requires detecting the multimode quadrature states with a local oscillator [10, 11, 23, 24], and probing the non-Hermitian lattice effects, which has not been achieved so far.

Remarkably, Kerr combs [13] (including dissipative Kerr solitons [25] and soliton crystals [26]) generated by third-order nonlinear resonators, naturally provide both pair production [27, 28] and coupling between the frequency modes through the process of Bragg scattering [5, 29–31]. These properties make Kerr combs a unique system to study multimode quantum phenomena [7, 32] and squeezing [33]. Interestingly, these Kerr combs also function as a multi-frequency pump (in contrast to a single pump [9]) which produces transport and amplification of the quantum fluctuations in the resonator, giving rise to “below-threshold” phase-locked combs [7]. The complexity of these squeezed combs, and their quadratic bosonic Hamiltonian, which includes parametric gain and coupling terms, has only recently begun to be treated theoretically [33, 34]. However, to date, such below-threshold multimode quadratures have not been measured directly, and it was not clear how these combs are related to quadrature lattices and the non-Hermitian lattice phenomena that govern them. Additionally the major development of dissipative Kerr microcombs, which has become the focal point of vast research efforts, offers new possibilities in shaping quantum light, but also

poses new limitations. Thus, studying the multimode quantum fluctuations generated by them is essential for both utilizing their quantum properties and gaining a better understanding of the quantum origin of their formation and their quantum noise limitations.

In this work, we experimentally study non-Hermitian lattice physics in photonic quadratures for the first time. Our quadrature lattice is formed by a tunable dissipative Kerr comb that couples different quadratures along the frequency dimension. We show theoretically and experimentally the relationship between dispersion symmetries and the quantum vacuum of the multi-frequency lattice states of the below-threshold comb. Our work explores theoretically Kerr combs exhibiting multimode squeezed states with robust single peak frequency structure and double peak structure, thereby revealing and manipulating novel mechanisms of Kerr comb formation. We then observe such multimode states experimentally by measuring the anti-squeezing and photon statistics of the below-threshold Kerr comb. Our work demonstrates how non-Hermitian lattice effects govern the below-threshold combs and the Kerr comb evolution and threshold crossing. To this end, we use the framework of non-Hermitian lattice physics and draw parallels with seminal classical non-Hermitian observations such as power oscillations caused by parity-time symmetry (PT symmetry) [15], and PT symmetric lattices [35–37]. This advancement can enable the generation of novel quantum optical resources on-chip, manipulation of quantum noise, and enhance the understanding of the quantum origin of Kerr comb formation.

## 2 Results

We consider a 2-FSR Kerr comb where every other cavity mode (every even-numbered cavity mode) is predominantly populated by coherent light, and light is pair-generated by the Kerr comb on all the other cavity modes (Fig. 1(a)). The loss in the odd cavity modes is greater than the parametric gain, such that these modes are populated by below-threshold light, *i.e.* a squeezed vacuum state. Each odd cavity mode is also directly coupled to neighboring odd modes (but not to the even modes) by Bragg scattering which originates predominantly from Kerr comb teeth separated in frequency by 2-FSR, creating a 1D lattice of frequency sites populated by vacuum states of light.

Such a scenario can be evoked either by injecting a comb, as depicted in Fig. 1a into a Kerr resonator, or by pumping the resonator with continuous-wave (CW) single frequency light, or multi-frequency light [38], causing the other comb teeth to emerge spontaneously via the symmetry-breaking phenomenon of Turing rolls [39] (Fig. 1(b)). The dynamics of the below-threshold light at the odd modes (centered around the pump at  $\mu = 0$ ) is given by the following Hamiltonian[7]

$$\hat{H} = \sum_{\mu} -\Delta\omega_{\mu}\hat{a}_{\mu}^{\dagger}\hat{a}_{\mu} - \frac{g_0}{2} \sum_{\mu,\nu,j,k} \delta[\mu + \nu - j - k] \left( A_{\mu}A_{\nu}\hat{a}_j^{\dagger}\hat{a}_k^{\dagger} + 2A_k^*A_{\nu}a_j^{\dagger}a_{\mu} + \text{h.c} \right) \quad (1)$$

where  $A_{\mu}$  are above-threshold amplitudes (the Kerr comb) in even cavity modes  $\mu$ ,  $\hat{a}_{\mu}^{\dagger}$  ( $\hat{a}_{\mu}$ ) are the creation (annihilation) operators of quantum light in odd cavity mode  $\mu$ , which are described in the rotating frame of reference of the Kerr comb  $U =$

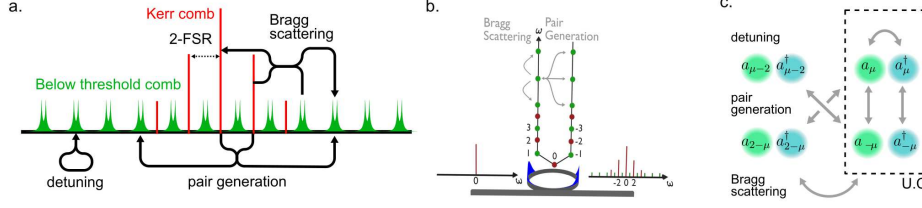


**Fig. 1 Squeezed quadrature lattices induced by Kerr combs.** **a.** A 2-FSR Kerr comb (red) and a generated sub-threshold multimode state with squeezing frequency structure (green). **b.** General scheme of the system: A Kerr ring resonator is pumped by CW light, generating a 2-FSR bright comb (red circles). This comb generates a sub-threshold comb (green circles), which has the connectivity of a 1D lattice by pair generation and Bragg scattering. **c.** A unit cell (U.C) of the 1D lattice in the bosonic creation and annihilation operator basis, longer range couplings decay with frequency distance.

$\exp(i\hat{R}t)$ ,  $\hat{R} = \sum_{\mu} (\omega_p + \Delta\Omega\mu) a_{\mu}^{\dagger} a_{\mu}$  where  $\Delta\Omega$  is the frequency spacing of the Kerr comb.  $\Delta\omega_{\mu}$  is the frequency detuning of the cavity-mode  $\mu$  from the Kerr comb frame of reference,  $g_0$  is the nonlinear coefficient, the Kronecker  $\delta$  reflects photon azimuthal wave number conservation in the system, and h.c stands for Hermitian conjugate.

To illustrate the quadrature lattice geometry, we plot the frequency axis in a “folded” form in which the pump is located at the edge (Fig. 1(b-c)). Thus a unit-cell in this lattice consists of four bosonic field operators  $a_{\mu}, a_{\mu}^{\dagger}, a_{-\mu}, a_{-\mu}^{\dagger}$ , which map to four field quadratures (see Methods 4.1 for the derivation of the quadrature lattice model). The simplified quadratic bosonic lattice model can be used both to understand the fundamental sub-threshold comb behavior and to engineer it. The sub-threshold quadrature dynamics of the Kerr comb constitutes a non-Hermitian 1D lattice [35–37, 40], which can be either APT symmetric (pseudo Anti-PT symmetric [16, 41]) or non-symmetric around the central point  $\mu = 0$ . In the APT symmetric case all the eigenvalues will be purely real or purely imaginary, while in the non-symmetric case they are complex. In a realistic Kerr micro-comb the APT symmetry is mainly eliminated by a mismatch between the Kerr comb frequency spacing ( $\Delta\Omega$ ) and the FSR of the cavity. As a consequence this mismatch can be designed to exhibit APT symmetry by dispersion engineering. To understand the impact of the APT symmetry on the quadrature lattice we reduce the number of parameters by writing the Hamiltonian for the odd cavity modes in a unitless form. Only two parameters need to be considered for the minimal model:  $\alpha$  which defines simplified comb amplitudes - decreasing at constant rate, by:  $A_{\mu}/A_0 = 10^{-\mathcal{R} \cdot |\mu|/10} \equiv \alpha, \mathcal{R} > 0$ , and  $\Delta\tilde{\omega}_{\mu}$  which is the unitless frequency detuning of the cavity modes from a rotating frame of reference aligned with the Kerr comb. To the first order of  $\alpha$  we obtain the following form for the lattice Hamiltonian:

$$\begin{aligned} \hat{H}_{\text{lat}} = & -g_0 A_0^2 \sum_{\mu \in \text{odd}, \mu > 0} \left[ \frac{1}{2} (\Delta\tilde{\omega}_{\mu} + 2) \hat{c}_{\mu}^{\dagger} \hat{c}_{\mu} + 2\alpha \hat{c}_{\mu}^{\dagger} \hat{c}_{\mu-2} \right] \\ & + \left[ \frac{1}{2} (\Delta\tilde{\omega}_{-\mu} + 2) \hat{d}_{\mu}^{\dagger} \hat{d}_{\mu} + 2\alpha \hat{d}_{\mu}^{\dagger} \hat{d}_{\mu-2} \right] + \left[ \hat{c}_{\mu}^{\dagger} \hat{d}_{\mu}^{\dagger} + 2\alpha \hat{c}_{\mu}^{\dagger} (\hat{d}_{\mu-2}^{\dagger} + \hat{d}_{2+\mu}^{\dagger}) \right] + \text{h.c} + \mathcal{O}(\alpha^2) \end{aligned}$$

(2)

where  $c_\mu \equiv a_\mu, d_\mu \equiv a_{-\mu}$  for  $\mu > 0$ , and  $d_{-1} \equiv c_1, c_{-1} \equiv d_1$ . We note that the higher order terms  $\mathcal{O}(\alpha^n)$  add Bragg coupling and pair generation terms to  $n$ -nearest neighbours thereby not breaking the lattice structure. In this “folded” representation it is possible to show that if the detuning  $\Delta\tilde{\omega}_\mu$  is symmetric around  $\mu = 0$ , the bosonic quadratic lattice in Eq. 2 becomes a degenerate pseudo APT symmetric lattice which results in a eigenspectrum with eigenvalues that are purely real or purely imaginary (Methods 4.1).

To describe realistic quantum noise behavior, the bosonic quadrature lattice of Eq. 2 must be finite, which naturally occurs due to group velocity dispersion (GVD) reducing the Bragg coupling coefficient for modes away from the center. If we define  $\Delta\tilde{\omega}_\mu = \Delta\tilde{\omega}_0 + \tilde{D}'_1\mu + \tilde{D}_2\mu^2/2 + \mathcal{O}(\mu^3)$ , then  $\Delta\tilde{\omega}_\mu$  is symmetric if all the odd terms are zero. Note that  $D'_1(\tilde{D}'_1)$  is the (unitless) frequency difference between the cavity FSR and the Kerr comb’s frequency spacing. To illustrate the implication of different  $D'_1$  values, we calculate the quadrature eigenspectrum of the sub-threshold light generated by a 2-FSR Kerr comb with fixed  $A_\mu$  profile and varying  $D'_1$ . For concreteness, we use  $\mathcal{R}$  and  $D_2$  taken from our experimental system (see Methods 4.2). Figure 2(a) shows the symmetric case in which  $D'_1 = 0$ , while Figs. 2b(c) are non-symmetric with  $D'_1/2\pi = 3(8)MHz$ . We adjust the overall comb power in the plots in Fig. 2 to be close to threshold for detuning  $\Delta\omega_0 = 2g \sum_\mu |A_\mu|^2$ . To compute the quadrature eigenspectrum we write Eq. 1 in the quadrature basis  $(p_1 \dots p_N, q_1 \dots q_N)$  where  $p_i$  and  $q_i$  are the quadratures of mode  $i$ , and  $N$  is the number of participating cavity modes. We obtain the dynamical matrix  $\mathcal{M}$  which is non-Hermitian. To study threshold behavior we introduce  $\Gamma = \kappa/2I_{2N \times 2N}$ , where  $\kappa$  is the uniform intensity loss rate.

In Fig. 2 we analyze the eigenspectrum of  $\mathcal{M} - \Gamma$  while varying the parameter  $D'_1$ , taking into account all orders of  $\alpha$ . We observe three distinct regimes. For  $D'_1 = 0$  (Fig. 2(a)), the eigenvalues are either purely real or have a real part that equals  $-\kappa/2$  resulting from their initial purely real eigenvalue shifted uniformly by  $\kappa/2$ . Interestingly, due to the multimode nature of the system, even when the symmetry is removed (*i.e.* when  $D'_1 \neq 0$ ) some states close to threshold remain with imaginary values of 0 (*i.e.* the partially symmetric case, see Fig. 2(b)). This gradual decrease in the number of purely real eigenvalues or robustness is analyzed in Methods 4.2. For the highest  $D'_1$  in Fig. 2(c), the modes close to threshold all have a double peak structure (*i.e.*, imaginary part is non zero).

Each eigenvalue in Fig. 2(a-c) represents a multimode squeezed state, residing on the odd modes. As depicted in green in Fig. 1(a) the squeezing spectrum of each supermode uniformly evolves around each cavity mode [33]. The spectral structure around each cavity mode is frequency dependent squeezing, a concept which recently started to be utilized in metrology application through noise spectrum engineering [42].

To compute the multimode frequency-dependent squeezing structure, we calculate the supermodes of  $\mathcal{M} - \Gamma$ , using the Bloch-Messiah decomposition (details in Methods 4.2). The structure of the supermodes with the highest real part (gain) in

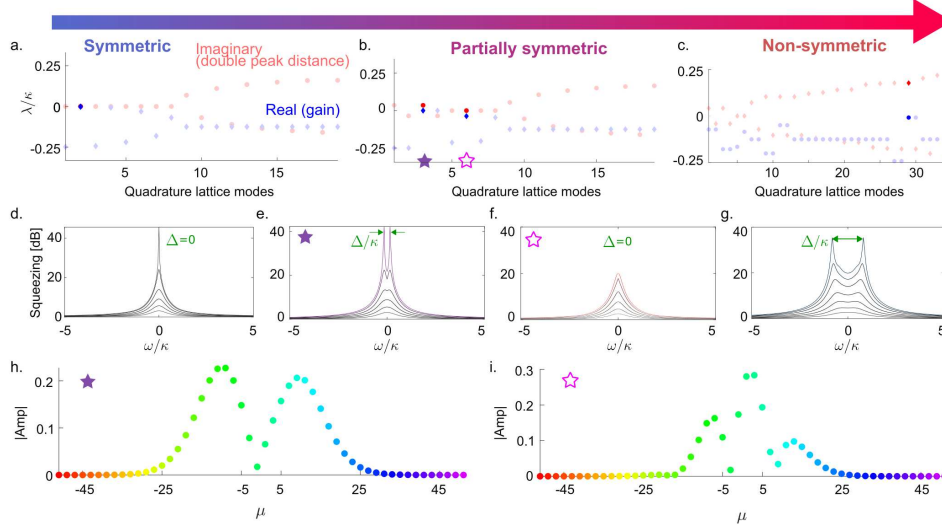


**Fig. 2 Dispersion symmetry and the properties of supermode squeezed states.** a.-c. Eigenvalues of the multimode states of a 2-FSR comb with different values of  $D'_1$ : 0, 3 and 8 MHz respectively. For larger  $D'_1$  the purely real eigenvalues gradually become complex. Highlighted quadrature supermodes are those close to threshold. d.-g. The frequency( $\omega$ )-dependent squeezing spectrum of the supermodes close to threshold (highlighted). Each line represents the supermode spectrum for a linearly swept intra cavity power, and the supermodes can be seen to narrow as they approach threshold. The supermode in f. does not narrow asymptotically because e. reaches threshold first. h.,i. The supermode composition as a function of cavity modes of the multimode squeezed states, for the supermodes in e. and f. respectively (colours correspond to the frequencies).

Fig. 2(a-c) is presented in Fig. 2(d-g). Supermodes with the highest gain will dominate in total photon number over other supermodes and have the narrowest peaks, being closest to the optical parametric oscillator (OPO) threshold. The OPO threshold occurs when  $Re(\lambda) = 0$ , where  $\lambda$  denotes the eigenvalue of the supermode with the highest real part. The frequency spacing in the double peak structure is determined by the imaginary value of the corresponding supermode by  $\Delta = 2Im\lambda$ . Therefore, supermodes with imaginary value zero, exhibit a single peak structure (“un-detuned” from the frame of reference of the Kerr comb), while supermodes with imaginary value that is not zero exhibit double-peak spectrum (“detuned” from the frame of reference of the Kerr comb).

The partially symmetric case shows how the transition between a dominant double peak supermode and single peak supermode is not continuous but is the result of supermode competition. It exhibits both double-peak and single peak evolution for different supermodes with high gain simultaneously. The different plotted lines in each spectral shape in Fig 2(d-g) represent the squeezing for different distances from threshold (by changing the overall power of the Kerr comb). Together with an intra-modal frequency-dependent structure, each supermode has a spectral structure in the cavity mode basis, shown for the partially symmetric case in Fig. 2(h-i). The

bandwidth of these supermodes is predominantly determined by the values of  $D'_1$  and  $D_2$ .

Next, we aim to experimentally observe the frequency-dependent quadrature variance directly for the different cases described above using integrated microring resonators [43]. In this work, we utilize 4H-silicon carbide-on-insulator [44], which offers low losses and high third-order nonlinearity, enabling low-power operation. We excite a localized 2-FSR Kerr comb by injecting CW light near an avoided mode crossing, generating strong local anomalous dispersion. The comb is naturally phase-locked via cascaded parametric processes and centered within the telecommunications c-band (1545 nm). The characterization of the device parameters, including dispersion, is presented in Methods 4.3 and Methods 4.5).

We begin by characterizing the modal structure of a generated 2-FSR supermode in its native basis. Using a custom-built single-photon optical spectrum analyzer (SPOSA)[7], which provides  $> 100$  dB of dynamic range with single-photon sensitivity, we simultaneously capture the photon populations above- and below-threshold, as shown in Fig. 3(a). Mapping out the two-photon correlation matrix of the below-threshold state can reveal the inter-modal connectivity in the Hamiltonian, and provide indications of the formation of the supermodes introduced in Fig. 1(b,c). We perform pairwise second-order photon correlation measurements,  $g_{ij}^{(2)}(\tau) = \langle \hat{a}_i^\dagger(0)\hat{a}_j^\dagger(\tau)\hat{a}_j(\tau)\hat{a}_i(0) \rangle / \langle \hat{a}_i^\dagger(0)\hat{a}_i(0) \rangle \langle \hat{a}_j^\dagger(\tau)\hat{a}_j(\tau) \rangle$  on each pair of below-threshold modes in the comb, and the resulting matrix is shown in Fig. 3(b). The signature of supermodes is seen as pair-wise correlations between modes close in their distance from the center pump mode (consistent with the folded picture in Fig. 1(b)).

In this work we aim to resolve the spectrum and behavior of single supermodes. The central 12 below threshold modes of Fig. 3(b) (modes -9,-7,...,13) are governed by a single supermode. This is evident from the time dependent analysis of all pairwise  $g_{i,j}^{(2)}(\tau)$  correlations for  $-9 < i, j < 13$ . Figures 3(c-e) show that both the auto-correlations (Fig. 3(c)) and cross-correlations (Fig. 3(d)) exhibit beating in frequency  $\Delta = 140 - 160$  MHz (Fig. 3(e)) with a bandwidth of 10 MHz, an order of magnitude less from the resonances linewidth. The correlations indicate that all modes are below the OPO threshold and are therefore squeezed on-chip. According to the theory presented in Fig. 3 all beatnotes should be the same. Indeed, the center frequency of the bandwidth is 10MHz and when the measured frequencies are ordered according to acquisition time (spanning several hours), it becomes clear that most of the variance is due to slow gradual shifts in the hot-cavity dispersion. These observations demonstrate the uniform noise spectrum of a Kerr comb vacuum supermode which is comprised of many modes, for the first time.

We further confirm the supermode structure, by performing a homodyne measurement on the different modes. Each plot in Fig. 3.(f-l) presents the double peak below threshold structure with of the supermodes with increasing proximity to threshold. The differences between the values of  $\Delta$  and the correlations - are due to the measurements taking place at different times. We proceed to demonstrate the transition between the non-symmetric regime and the symmetric regime through continuous tuning of the resonator dispersion properties. Gradually heating the microring changes the mode splitting, and therefore the threshold point, allowing us to vary  $D'_1$  and as



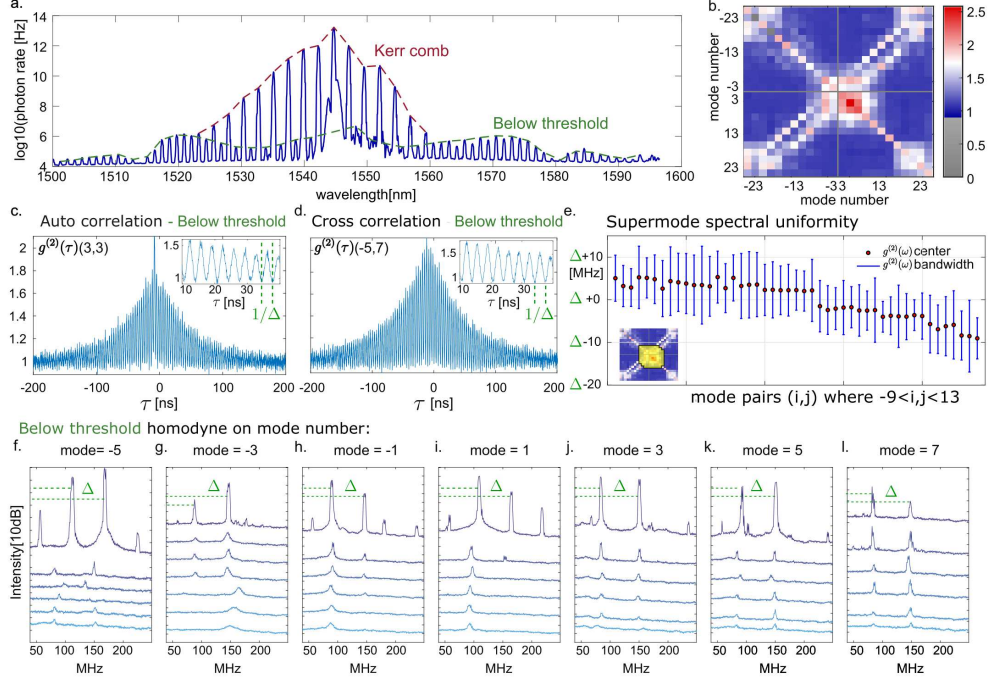


**Fig. 3 Observation of a single supermode with 10 modes** **a.** Single-photon optical spectrum analyzer (SPOSA) measurement of photon populations in above threshold (red) and below threshold (green) modes of the 2-FSR state. **b.** The two-photon correlation ( $g^{(2)}$ ) matrix of the below threshold light in the odd modes, showing the correlations generated by Bragg scattering and pair-generation in the quadrature lattice. **c.,d.** Auto correlation and cross correlation as a function of time-delay of the mode pairs (3,3) and (-5,7) showing temporal broadening indicating squeezing, and the inner frequency  $\Delta$  of the detuned supermode. **(e)** The frequency  $\Delta$  and the bandwidth (temporal broadening) of all the odd mode pairs between -9 and 13. The pairs are sorted according to acquisition time, showing that the main deviations from a constant frequency is due to hot cavity dispersion gradually changing with time. **f.-l.** Homodyne measurements near the odd cavity modes, gradually approximating the secondary comb threshold showing the evolution of the uniform double peak noise structure as it approaches threshold.

a consequence  $\Delta$  (see Methods 4.3). Tuning our below-threshold comb above threshold, we observe through homodyne detection that adjusting the voltage of the heater changes the secondary comb frequency structure above threshold discontinuously (Methods 4.4). Figure 4(a-c) shows the above-threshold peaks for different applied voltages. We observe three distinct voltage regimes: In the first, the threshold presents a double peak structure with the peak separation of approximately 300 MHz (Fig. 4(a)), significantly larger than the cavity linewidth of 100 MHz, thus corresponding to the strongly non-symmetric regime of Fig. 2(c,g) and Fig. 3. Further tuning the voltage (Fig. 4(b)), we transition discontinuously to a regime in which the detuning is small, around 30 MHz, which corresponds to the partially symmetric regime of Fig. 2(b,e,f) followed by a transition to a single peak (corresponding to the symmetric case threshold crossing of Fig. 2(a,d)). The discontinuous change of the frequency spectrum with



the voltage occurs because each regime in Fig. 2 corresponds to a different supermode crossing threshold, which is not a continuous process. Afterward, the system abruptly transitions to the partially-symmetric state again. This matches completely to the regimes described in Fig. 2.

To observe the competing multimode processes in the quantum regime, we also measure the below-threshold quadrature vacuum fluctuations (anti-squeezing), whose evolution precedes the formation of the above-threshold light shown in Fig. 4(a-c). To observe the below-threshold light, we reduce shot noise using on-chip and off-chip filters (Methods 4.3). Furthermore, we tune the power ratio of our two-tone LO of modes -1 and 1 to a ratio of  $LO_1 = 10 \cdot LO_{-1}$ , which we found to maximize the overlap with the amplified quadrature supermode.

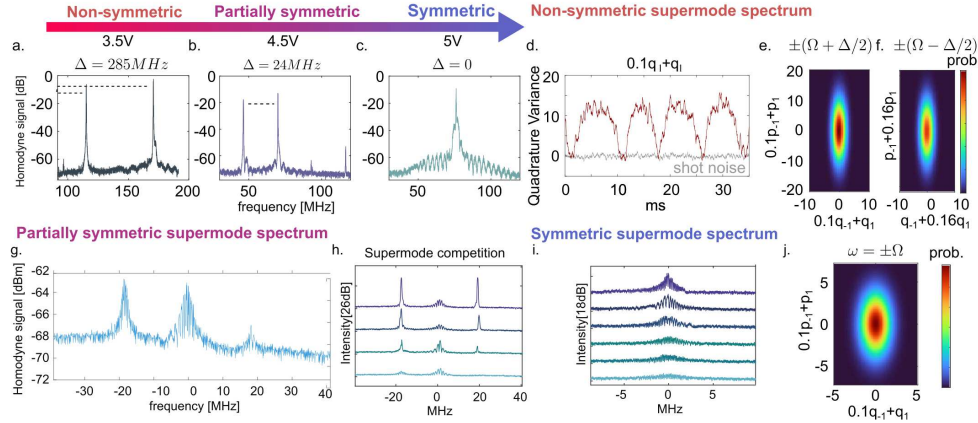


**Fig. 4 Exploring quadrature structure for different non-Hermitian symmetry regimes**  
**a.-c.** Homodyne measurements for three different applied heater voltages, showing the different regimes from symmetric to non-symmetric (dashed line corresponds to  $\Delta$ ) **d.** quadrature variance (in dB) of the detuned supermode, measured using a two tone LO with temporal phase sweeping. **e.-f.** reconstructed quadrature probability for two pairs of squeezed peaks  $\pm(\Omega + \Delta/2)$  and  $\pm(\Omega - \Delta/2)$  respectively. **g.** Below-threshold quadrature oscillations induced by a phase shifter, demonstrating the co-existence of two quadrature supermodes - detuned and non-detuned simultaneously, indicating the partially symmetric regime. **h.** Tuning closer to resonance from (g) shows the detuned state increasing in gain while the non-detuned state remains weak, confirming the presence of two competing quadrature supermodes. **i.** Quadrature variance of the non-detuned peaks, showing the variance profile of the non-detuned quadrature supermode. **j.** Reconstructed quadrature probability of the non-detuned mode based on a pair of squeezed peaks  $\pm\Omega$

Figure 4(d) presents the stretched quadrature structure of the detuned supermode as we temporally sweep the phase of the LO. The modes -1 and 1 contain four peaks out of approximately 24 peaks that compose the entire supermode. Fig.4(e,f) shows the stretched quadrature structure in quadrature space of 2 pairs out of the four. Next we position the comb at a quite 2-FSR soliton crystal stage for which the  $\Delta$  is smaller. The small  $\Delta$  corresponds to the partially symmetric case (Fig. 2(b,e,f)). In Fig. 4(g), we observe both the single peak and double peak supermodes of Fig. 2(b,e,f) simultaneously. By further red-tuning the input pump frequency, we observe the competing dynamics in which the detuned supermode is amplified and narrows further until it

crosses threshold, the non-detuned supermode does not (Fig. 4(h)). This physics is described by the simplified non-Hermitian lattice model which our comb approximates to, providing a powerful tool to understand the physics of the vacuum noise of Kerr combs.

We emphasize that the non-detuned supermode was not predicted theoretically in any treatment of multimode supermodes of Kerr combs, since it requires the non-Hermitian anti PT symmetry which generically does not exist in Kerr combs. Focusing further on the non-detuned state (Fig. 4(i)), we measure the stretched quadrature structure (Fig. 4(j)). In principle, the spectrum structure of the anti-squeezing is equivalent to that of the squeezing, but more robust to losses making it useful for exploration. This property allows exploration of quadrature lattice without observing below shot-noise variance directly. Using these states as a squeezed quantum resource would require overcoupling to the resonator and utilizing a LO with higher bandwidth, along with very low out-coupling losses.

The co-existence of quadrature supermodes and the robustness of single-peaked supermodes have significant implications for the process of comb formation and evolution: The two-peaked sub-threshold gain profile dictates the secondary comb frequency structure. It predicts the formation of classical beatnotes but not through the mechanism of sub-combs frequency mismatch which occurs in other circumstances. [45]. It is revealing to understand how the different types of anti-squeezing structures affect the threshold from primary 2-FSR comb to a 1-FSR secondary comb. Before presenting the experimental results, we wish to gain further insights from the Lugiato–Lefever equations (LLE) [46] and simulate the classical non-linear evolution at the threshold (see LLE simulation details in Methods 4.5). By tuning the quality factors and dispersion in the simulation to impose a small  $D'_1$ , we can simulate a secondary comb threshold that does not generate rf beatnotes [45](Fig. 5(a-b)). In this type of threshold, the 2-FSR comb turns into a 1-FSR comb as a result of a dominant symmetric supermode. Therefore, only after the first threshold to an un-detuned 1-FSR comb, a second threshold of a detuned comb occurs between the 1-FSR comb and an additional 1-FSR comb, which in-turn leads to an rf beatnote and transmission fluctuations Fig. 5(b). We emphasize that symmetric quadrature lattices can be generated in a variety of nonlinear approaches, that cannot all be explored in this manuscript. Thus, other nonlinear steady states that produce several pumps will also behave similarly.

Returning to our experiment, we follow the sub-threshold light with the same homodyne measurement as in Fig. 4(a). We take multiple snapshots of the quadrature structure during the process of threshold crossing. In Fig. 5(c), we observe how the non detuned sub-threshold anti-squeezed light crosses the threshold. The first threshold crossing results in a 1-FSR comb, and no rf beatnote. This is followed by a second quadrature supermode, this time detuned, crossing the threshold and giving rise to sub-combs (Fig. 5(d)). One can clearly see that after the threshold crossing of the un-detuned mode, the detuned mode still exists and keeps growing until it also crosses the threshold. Thus, our measurements reveal the mechanism for creating a 1-FSR comb from a 2-FSR primary comb without formation of an rf beatnote. The case of the un-detuned threshold contrasts with the case in which the detuned quadrature

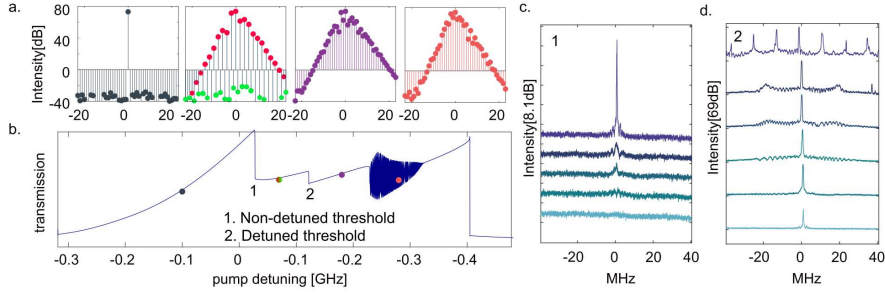


**Fig. 5 Primary to secondary threshold behavior of a non-detuned (symmetric) quadrature supermode.** **a-b.** LLE simulation of a non detuned supermode that crosses threshold and becomes a secondary 1-FSR comb. The simulation shows that it is followed by a second threshold in which a detuned state crosses threshold, which is then followed by the generation of light that causes an rf beatnote and transmission oscillations. **c-d.** The experimentally observed evolution of a non-detuned supermode into a secondary comb in the symmetric regime; c. shows the first threshold (1) of a, d. is the second threshold (2) that follows c and is detuned.

supermode reaches threshold first. In that case, as we show in Fig. 3(f-i), a comb with an rf beatnote can appear immediately after the first threshold.

### 3 Discussion

In this work we demonstrated non-Hermitian lattice effects in photonic multimode quantum fluctuations described as photonic quadrature lattices. We used Kerr combs that generate photonic quadrature lattices to experimentally explore their non-Hermitian properties for the first time. By controlling the resonator dispersion via an integrated microheater, we were able to observe the three regimes predicted by the lattice model corresponding to different non-Hermitian lattice behavior. Namely, we observed the symmetric case, partially symmetric, and non-symmetric. Kerr combs allow scalability and rich complexity on a compact on-chip platform. By measuring the anti-squeezing of 2-mode projection of the quadrature supermode, we revealed the existence of detuned and robust non-detuned squeezed supermodes and explained how these form in the context of lattice symmetries. Exploring such fundamental properties paves the way for designing more complex lattice phenomena by injecting or probing different above-threshold states, for example states with nontrivial artificial gauge fields such as topological combs [47]. Additionally, other pump schemes can lead to non-trivial gauge fields in the quadrature space, leading to non-reciprocal quadrature flow. Furthermore, understanding comb formation and the quantum noise of Kerr combs with our approach can lead to improved comb technology, particularly for combs that are governed by quantum noise which dictates the ultimate limit on comb stability. The concepts studied here form a bridge that will enable the exploitation of the rich non-Hermitian lattice physics in quadrature bosonic lattices to engineer complex quantum resources on-chip. The complex transport of quadratures offered by the Kerr effect and demonstrated in this work will lead to lattice phenomena such as non-Hermitian skin effect, Anderson localization, edge-states and topological phases.

These phenomena would manifest as quadrature modes offering new opportunities to control quantum light.

## 4 Methods

### 4.1 Band model for quadrature lattice induced by a Kerr comb

As shown in Eq. 2 in the main text, 2-FSR Kerr combs generate 1D quadrature lattices on the frequency axis. The lattice geometry allows reducing the complexity of modeling the physics from a general network of quadratures to a 1D lattice geometry. The goal of this section is to explain the physics of the quadrature lattice by deriving an analytical expression for the band model of the quadrature lattice and its Brillouin zone. First, we transform the Hamiltonian in Eq. 2 into the quadrature basis  $\vec{R} = (p_{-N}, \dots, p_N, q_{-N}, \dots, q_N)^T$  where  $p_\mu = \frac{1}{\sqrt{2}}(a_\mu^\dagger + a_\mu)$ ,  $q_\mu = \frac{i}{\sqrt{2}}(a_\mu^\dagger - a_\mu)$  and write the quadrature non-Hermitian Hamiltonian  $\mathcal{M}$  [48], which satisfies the Heisenberg equation:

$$\frac{\partial \vec{R}}{\partial t} = \mathcal{M} \vec{R} \quad (3)$$

We obtain translation symmetry of the lattice by assuming periodic boundary conditions and flat dispersion  $\Delta\tilde{\omega}_\mu$  in the folded lattice, meaning that  $\Delta\tilde{\omega}_\mu = \tilde{\delta}_A\Theta(\omega - \mu) + \tilde{\delta}_B\Theta(\omega + \mu)$  where  $\Theta$  is the step function and  $\tilde{\delta}_{A(B)}$  are real numbers. We again use the operators  $\hat{c}_\mu, \hat{d}_\mu$  and their appropriate quadratures:  $\hat{p}_{c,\mu}, \hat{q}_{c,\mu}, \hat{p}_{d,\mu}, \hat{q}_{d,\mu}$ . The difference  $\tilde{\delta}_A - \tilde{\delta}_B$  creates an asymmetry in the dispersion  $\Delta\tilde{\omega}_\mu$  which removes the anti-parity symmetry, thus it functions as a simplified representation of the mismatch  $D'_1$ . By using the translation symmetry, we transition to the reciprocal space defined by the good quantum number  $k$ , obtaining a  $4 \times 4$  Hamiltonian:

$$\mathcal{M}_k = \begin{pmatrix} 0 & g_{A,k} & 0 & f_k \\ -g_{A,k} & 0 & f_k & 0 \\ 0 & f_k & 0 & g_{B,k} \\ f_k & 0 & -g_{B,k} & 0 \end{pmatrix} \begin{pmatrix} \hat{p}_{d,k} \\ \hat{q}_{d,k} \\ \hat{p}_{c,k} \\ \hat{q}_{c,k} \end{pmatrix} \quad (4)$$

where the variables  $g_{A(B),k} = (\tilde{\delta}_{A(B)} + 2) + 2\alpha e^{ik} + 2\alpha e^{-ik}$  originate from the dispersion, Bragg scattering, and self phase modulation, while  $f_k = -1 - 2\alpha e^{ik} - 2\alpha e^{-ik}$  are pair generation terms, and  $\mathcal{M} = \sum_k \mathcal{M}_k + \mathcal{O}(\alpha^2)$ . The Hamiltonian  $\mathcal{M}_k$  has pseudo anti-parity symmetry (implying that the eigenvalues of  $\mathcal{M}_k$  are either purely real or purely imaginary) if  $\tilde{\delta}_A = \tilde{\delta}_B$ , which shows why there exist a detuned threshold when  $\Delta\tilde{\omega}_\mu$  is not symmetric around  $\mu = 0$ .

Therefore, by considering the case in which  $\tilde{\delta}_A = \tilde{\delta}_B \equiv \tilde{\delta}$  the quadrature Hamiltonian  $\mathcal{M}_k$  becomes degenerate. We simplify the treatment further by transitioning to a new quadrature basis in the unit cell according to  $\vec{R}' = U\vec{R}$  where

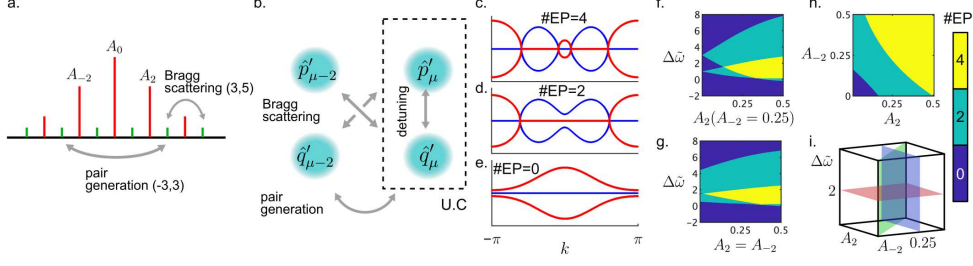


**Fig. 6 2-band model of a quadrature lattice induced by a 2-FSR Kerr comb.** **a.** Illustration of the above threshold comb (red) and below threshold comb (green) in the model, and of the different terms - pair generation and Bragg scattering that couple the different modes. **b.** The 1D lattice unit cell, in the generalized quadrature basis  $(\hat{p}'_\mu, \hat{q}'_\mu)$ . **c-e.** Different band topologies (different number of exceptional points) of the Brillouin zone of the lattice in **b**, plot **c** corresponds to  $A_{\pm 2}/A_0 = 0.25$ ,  $\Delta\tilde{\omega} = 2$ , plot **d** corresponds to  $A_2/A_0 = 0.25$ ,  $A_{-2}/A_0 = 0.2$ ,  $\Delta\tilde{\omega} = 2$  and plot **e** to  $A_{\pm 2}/A_0 = 0.25$ ,  $\Delta\tilde{\omega} = 0$ . **f-i.** The number of exceptional points for different 2-FSR Kerr combs on different slices of the 3D parameter space. The parameter space is spanned by the two ratios of the sidebands and the overall detuning.

$\vec{R}' = (p'_{1,k}, q'_{1,k}, p'_{2,k}, q'_{2,k})$  is a generalized quadrature basis, and the unitary is:

$$U = \frac{1}{4} \begin{pmatrix} 1 & 1 & -1 & 1 \\ -1 & 1 & -1 & -1 \\ 1 & 1 & 1 & -1 \\ -1 & 1 & 1 & 1 \end{pmatrix} \quad (5)$$

Applying the change of coordinates with  $U$  leads to the following 2 by 2 Hamiltonian:

$$\mathcal{M}'_k = \begin{pmatrix} 1 + 2\alpha e^{ik} + 2\alpha e^{-ik} & (\tilde{\delta} + 2) + 2\alpha e^{ik} + 2\alpha e^{-ik} \\ -(\tilde{\delta} + 2) - 2\alpha e^{ik} - 2\alpha e^{-ik} & -1 - 2\alpha e^{ik} - 2\alpha e^{-ik} \end{pmatrix} \quad (6)$$

which is related to  $\mathcal{M}_k$  of Eq. 4 by  $\mathcal{M}_k = U^\dagger \mathbf{I}_{2,2} \otimes \mathcal{M}'_k U$ . The 2-band model of Eq. 6 represents the most basic lattice quadrature physics and is pseudo Hermitian with APT symmetry. This means that its eigenvalues are either purely real or purely imaginary and it has exceptional points for appropriate lattice parameters. To illustrate the APT symmetry consider the operators  $\mathcal{P} = \sigma_x$  and  $\mathcal{T} = K$ , where  $\sigma_x$  is the x Pauli matrix, and  $K$  is the conjugation operator. These operators  $\mathcal{PT}$  and  $\mathcal{M}'_k$  are anti-commuting:  $\{\mathcal{PT}, \mathcal{M}'_k\} = 0$  which shows the APT symmetry.

Due to the degeneracy, we use only two variables:  $(p'_k, q'_k)$ , allowing us to explore some of the fundamental physics of our lattices. Figure 6 analyzes the 2-band model of Eq. 6. Figure 6(a) shows different non-linear terms and the structure of the comb (red) and sub-comb(green), while Fig. 6(b) presents the folded representation where translation symmetry exists.

Next, we analyze the parameter space of the comb shown in Fig. 6(a) where  $\alpha < 0.5$ . In this parameter sub-space there can exist 0,2 or 4 exceptional points in the Brillouin zone (Fig. 6(c-d)). We map the 3D parameter space for combs (also for combs with

$A_2 \neq A_{-2}$ ) presenting the different band topologies (Fig. 6(f-i)). We note that having 4 exceptional points is not an inherent maximum; beyond the presented parameter space, more exceptional points can exist. Additionally, the relative phases between the comb tones can influence the number of exceptional points when more than two pumping amplitudes are considered. Therefore, while we provide the basic mechanisms governing such lattices, they can become significantly more complex. The analysis of the 2-band or 4-band models sheds light on the eigen-vector and eigen-value structures. However, the infinite lattice cannot reach threshold by definition and is therefore not suitable for studying multi-mode squeezing phenomena on its own, and must be truncated for that purpose. More details on the truncation and its implication on the results of the 2-band model will be discussed in the next section.

## 4.2 The finite model and analysis of the robustness of non-detuned quadrature lattice modes

In this section, we continue with the theoretical analysis akin to Methods 4.1 focusing on finite lattices. Similar to structures in physical space, a realistic lattice in the frequency domain is inherently finite. Naturally, dispersion is never completely flat (i.e group velocity dispersion or higher-order terms are never zero), implying that as the lattice extends towards higher and lower frequencies away from the pump, the detuning between the cold cavity dispersion and the quadrature lattice modes increases. This effect reduces the coupling efficiency of Bragg scattering and possibly pair generation, leading to “soft edges” and resulting in a gradual decrease in transport between frequencies. In contrast, edges can also be made abrupt through engineering of mode crossing or other type of frequency dependent defects [20]. These sharp edges can be desirable as they may host confined edge-states in the synthetic frequency dimension [49]. While Kerr resonators can accommodate both options, our focus here is on naturally occurring edges due to non-zero group velocity dispersion.

Furthermore, we will numerically demonstrate that the non-detuned multimode states persist even when dispersion is non-flat and are robust against the breaking of dispersion symmetry around the pump frequency  $\mu = 0$ . Starting from Eq. 2, we assume  $\Delta\tilde{\omega}_\mu = \omega_p + D'_1\mu + D_2\mu^2$ , where  $D'_1 = \Delta\Omega - D_1$  and  $D_1$  represents the FSR. When  $D_2 \neq 0$  and/or  $D'_1 \neq 0$  the multimode states localize, allowing us to analyze them using a finite Hamiltonian  $\mathcal{M}$ . For this analysis, we assume equal quality factors for all resonances  $\Gamma = \kappa/2\mathbf{I}_{2N \times 2N}$ . Since  $\Gamma$  is real and proportional to the unit matrix, it only translates the real part of the eigenspectrum of  $\mathcal{M} - \Gamma$ , and does not influence the imaginary part of the eigenvalues or the peak separation of the squeezed multimode states. Following the conventions in [48] the input-output relation of the system and its Fourier transform are given by:

$$\frac{d\mathbf{R}_{out}}{dt} = (-\Gamma + \mathcal{M}) \mathbf{R}(t) + \sqrt{2\Gamma}\mathbf{R}_{in}(t) \quad (7)$$

$$\mathbf{R}_{out}(\omega) = S(\omega) \mathbf{R}_{in}(\omega) \quad (8)$$

The linear response matrix  $S(\omega)$  describes in our case how the system amplifies and squeezes the quantum fluctuations in the quadrature lattice and is given by:

$$S(\omega) = \sqrt{2\Gamma} (i\omega\mathbf{I} + \Gamma - \mathcal{M})^{-1} \sqrt{2\Gamma} - \mathbf{I} \quad (9)$$

The matrix  $S(\omega)$  can be decomposed by the Bloch-Messiah decomposition which leads to:

$$S(\omega) = U(\omega) D(\omega) V^\dagger(\omega) \quad (10)$$

where the matrices  $U$  and  $V$  are unitary and  $D(\omega) = \text{diag}\{d_1(\omega), \dots, d_N(\omega) | d_1^{-1}(\omega), \dots, d_N^{-1}(\omega)\}$  corresponds to squeezing and anti-squeezing values of the different quadrature supermodes. Next we aim to show more broadly the impact of group velocity dispersion and asymmetry in dispersion relative to the comb on the multi-mode states. In Fig. 7(a-b) we present a typical complex eigenvalue band structure for a quadrature lattice with  $D_2 \neq 0$ , setting  $D_2/2\pi = 1.2 \text{ MHz}$ ,  $\mathcal{R} = 2.25$ , and  $Q_i = 1.74 \cdot 10^6$ , which are experimental parameters also used in Fig. 2 of the main text. Clearly, dispersion compresses the spectrum bandwidth of the quadrature supermode and the number of participating supermodes. By focusing on the most relevant supermodes, we observe that APT symmetry persists: Supermodes are either purely real (un-detuned) or purely imaginary (detuned), with the purely real ones exhibiting higher gain.

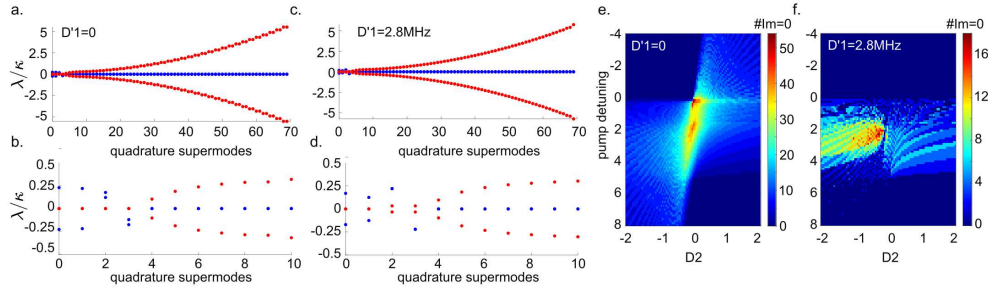


**Fig. 7 Existence of non-detuned state in the presence of non-zero  $D_2$  and  $D'_1$**  **a.** Eigenvalue solution of the quadrature Hamiltonian  $\mathcal{M}$  for a 2-FSR Kerr comb with side band drop ratio of  $\mathcal{R} = 2.25$ , and  $D_2/2\pi = 1.2 \text{ MHz}$ . **b.** Zoom-in on the quadrature supermodes with higher-gain showing that all of them are undetuned (imaginary value is 0.) **c-d.** Same as a. and b. only with  $D'_1/2\pi = 2.8 \text{ MHz}$ . **e.-f.** Numerically counting the un-detuned states as a function of underlying GVD ( $D_2$ ) and detuning of the comb for the symmetric case of  $D'_1 = 0$  and the non-symmetric case  $D'_1/2\pi = 2.8 \text{ MHz}$

Introducing a mismatch between the cavity FSR and the Kerr-comb frequency spacing eliminates lattice symmetry, yielding more general complex eigenvalue solutions for the  $\mathcal{M}$  matrix. When the mismatch is sufficiently small, as depicted in Fig. 7(c-d), we observe that some supermodes remain with purely real eigenvalues while others do not. Figure 7(e,f) shows the existence of un-detuned (imaginary eigenvalue is 0) supermodes as a function of  $D_2$  and constant pump detuning. Figure 7(e) enumerates supermodes with purely real eigenvalues for  $D'_1 = 0$ , while Fig. 7(f) counts the supermodes when  $D'_1/2\pi = 2.8 \text{ MHz}$ .



### 4.3 Additional data on fabricated device and experimental setup

Our devices are etched from a 550 nm thick 4H-SiC-on-Insulator [44] and capped with SiO<sub>2</sub>. Microheaters are patterned via liftoff of 100 nm platinum with a 5 nm titanium adhesion layer. Coupling to and from the chip is achieved using lensed fibers, with collection efficiency of up to 50%. The ring resonators exhibit intrinsic quality factors

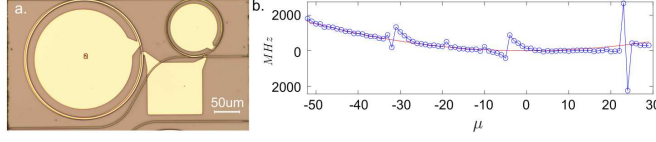


**Fig. 8 Micro-ring resonator: fabrication and dispersion.** **a.** Optical image of the Kerr ring resonator alongside the smaller on-chip filter ring and heaters. **b.** Integrated dispersion of the TE mode of the Kerr ring resonator (blue) and fit to  $D_2 = 1.2 \text{ MHz}$ ,  $D_1 = 152.7 \text{ GHz}$  (red). Dispersion defects are avoided mode crossings with other mode families.

of up to 8 million, with typical values around 1.5 million. The resonators exhibit a  $D_2/2\pi$  of 1.2 MHz, and an FSR of 153 GHz. Additionally, the ring is multimode, causing mode splitting through modal interactions (Fig. 8(b)), which allows a broad range of narrow-bandwidth states to be observed in the devices, such as 2-FSR primary combs (Fig. 9(a-b)), as well as the transition to 1-FSR combs and soliton crystals. The heaters modify the mode-splitting properties, thereby altering the detuning at threshold and consequently the Kerr comb's frequency spacing  $\Delta\Omega$ . Figure 9 presents the experimental evolution of the comb for the symmetric case. The comb starts as a 2-FSR primary comb (Fig. 9(a-b)) and undergoes an undetuned (single peak) threshold to a 1-FSR phase locked comb (Fig. 9(c)). Following the threshold, a second detuned (double peak) threshold occurs followed by additional thresholds and an rf beatnote in the comb (Fig. 9(d,e)). Finally, the comb abruptly turns to a 2-FSR soliton crystal (Fig. 9(f)).

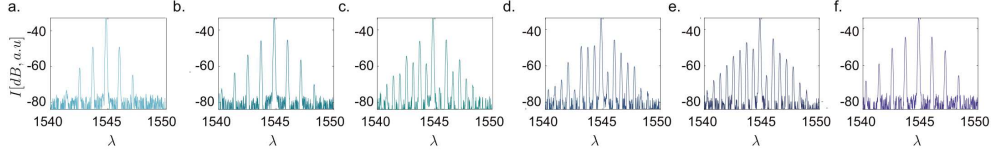


**Fig. 9 Kerr comb for different pump detuning - a single evolution.** **a.-b.** A 2-FSR primary comb, where b. is closer to the secondary threshold (the pump is at a longer wavelength) than a. **c.** Tuning the pump to longer wavelengths, the 2-FSR comb evolves to a single phase locked 1-FSR comb corresponding with Fig. 5(c-d). **d.-e.** Additional thresholds creating additional 1-FSR combs with subcombs corresponding with Fig. 5(d). **f.** Red tuning the pump further results in a 2-FSR soliton crystal (corresponding with the measurements in Fig. 4)

Next, we provide a more detailed description of the experimental setup (Fig. 10(a-b)). We utilize two tunable CW telecom lasers named CW laser 1 (Velocity, 1520-1570

nm, TLB-6728) and CW laser 2 (Toptica CTL1500: 1460-1570nm). The lasers are split into two channels. The first channel (upper channel in Fig. 10(b)) receives light from laser 1 and after amplification through an EDFA excites the Kerr resonator. The Kerr resonator outputs two channels: the first carries the quantum signal with the filtered Kerr comb directly to the homodyne unit, while the second channel contains the Kerr comb passing through the filter ring to a photodiode.

The second channel (bottom in Fig. 10(b)), receives light either from CW laser 1 or CW laser 2 or both. CW laser 1 is used for measuring modes -1 and 1, while CW laser 2 allows measuring other modes but is not phase-locked to CW laser 1. To

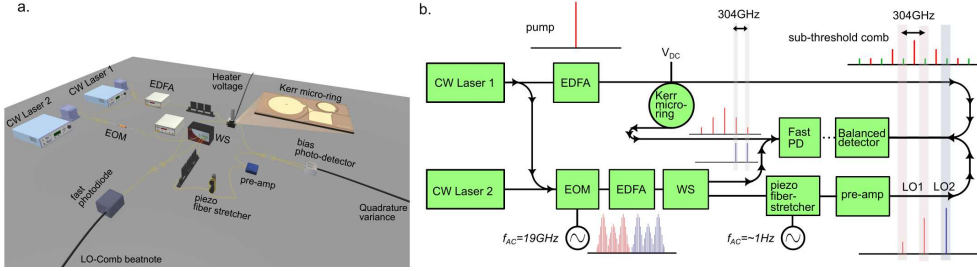


**Fig. 10 Principle components of the full experimental setup for quadrature variance measurements.** **a.** Realistic illustration of the table top setup. **b.** Schematic diagram of the setup presented in a. the abbreviations are: EDFA- erbium doped amplifier, EOM- electro-optic modulator, WS- waveshaper, PD- photodiode, pre-amp- low-power EDFA,

span a 3-FSR range with our LO, we employ an electro-optic modulator (EOSpace LiNbO3 20GHz phase modulator). Subsequently, a programmable WaveShaper (4000A multiport optical processor) transmits specific sidebands that overlap with the modes of the Kerr comb, filtering out all other lines. The frequency tones that overlap with the classical comb are mixed with the teeth that pass through the filter ring in order to track the frequency difference between the Kerr comb and the LO (center of the diagram in Fig. 10(b)). The frequency tones of the LO that overlap with the quantum signal are passed through a piezo fiber stretcher that stretches the fiber to change the phase of the LO. This continuous phase ramp is imprinted on the homodyne signal, allowing to distinguish it from other non-phase dependent fluctuations. The signal is then amplified with a low input power EDFA (OptiLab-MSA Pre-Amp EDFA Module, C-band) and then mixed with the quantum signal from the Kerr comb and fed into a balanced photodetector pair (WL-BPD1GA 1 GHz Dual-Balanced InGaAs Low Noise), to perform the homodyne measurement.

#### 4.4 Multimode Homodyne detection

To measure the maximal squeezing and anti-squeezing of the multimode below-threshold light, balanced homodyne detection must be performed with a multi-tone local oscillator (LO). The intensity and relative phase of each line of the LO should match the maximally-squeezed supermode of the squeezed vacuum [10]. In this work, the multi-tone LO is generated from a 20 GHz EOM comb [50] driven by the same

pump laser. The low bandwidth of a single phase modulator (or a few cascaded phase modulators) requires either working with relatively large micro-resonators or only partial overlap with the maximally squeezed supermode. Large micro-resonators pose additional challenges, including higher operation powers (for the same intrinsic quality factor) and a lower  $D_2$  for the same resonator cross-section. The theory and experimental validation we present in this work does not overlap optimally with the squeezed supermode, but is sufficient to capture the frequency-dependence of the most squeezed states. Therefore we are able to use a two-tone local oscillator despite the fact that the connectivity expands beyond two modes. We found that the two-tone local oscillator measures significantly stronger quadrature variance signal than a single-tone local oscillator by improving the overlap with the squeezed mode. Additionally, the two-tone symmetric LO may measure a time-independent phase relative to the signal in the absence of active phase locking of the EOM comb to the repetition rate of the Kerr comb [51].

We now provide further mathematical details on the multi-tone homodyne measurement.

To calculate the noise variance spectrum for a multi-tone local oscillator at the repetition rate of the comb [33], we can define a supermode decay operator

$$\hat{L}(t) = \sum_j \alpha_j \hat{a}_j(t) \quad (11)$$

whose Hermitian conjugate creates a photon in a superposition of azimuthal modes  $\hat{a}_j(t)$  across the frequency comb.  $\alpha_j = |\alpha_j|e^{i\phi_j}$  defines the amplitude and phase composition of the supermode. Its associated supermode output operator is

$$\hat{L}_{\text{out}}(t) = \sum_j \alpha_j \hat{b}_{\text{out},j}(t) \quad (12)$$

where  $\hat{b}_{\text{out},j}(t)$  is the output operator of mode  $\hat{a}_j(t)$ . The corresponding Hermitian quadrature operators of  $\hat{L}_{\text{out}}$  are:

$$\hat{L}_{\text{out}}^{(+)}(t) = \frac{1}{\sqrt{2}}(\hat{L}_{\text{out}}^\dagger(t) + \hat{L}_{\text{out}}(t)) \quad (13)$$

$$\hat{L}_{\text{out}}^{(-)}(t) = \frac{i}{\sqrt{2}}(\hat{L}_{\text{out}}^\dagger(t) - \hat{L}_{\text{out}}(t)) \quad (14)$$

The noise variance is then defined as

$$V^{(\pm)}(\omega) = \int_{-\infty}^{\infty} d\tau \langle \hat{L}_{\text{out}}^{(\pm)}(t) \hat{L}_{\text{out}}^{(\pm)}(t + \tau) \rangle e^{i\omega\tau}. \quad (15)$$

The maximally-squeezed supermodes can be obtained from the columns of  $U(\omega)$  (Eq. 10), which defines the linear combination of quadratures

$(q_1(t), \dots, q_n(t) | p_1(t), \dots, p_n(t))^T$  for a given supermode. When  $U(\omega)$  is real, then the composition for the  $k$ th maximally-(anti)squeezed supermode at  $\omega$  may be written:

$$|\alpha_j| = \sqrt{U_{j,k}(\omega)^2 + U_{j+n,k}(\omega)^2} \quad (16)$$

$$\phi_j = \text{atan2}(U_{j+n,k}(\omega), U_{j,k}(\omega)) \quad (17)$$

The quantum (anti)-squeezing is therefore significant when the local oscillator composition overlaps significantly with a multimode state that has large value  $d_i(\omega)$ . In this approach maximum quadrature variance can be obtained through this method for the undetuned squeezing. Since the undetuned squeezing occurs at  $\omega = 0$ , the value of its eigenvector is real  $U(0) \in \mathbb{R}$  and a time-independent local oscillator (in the frame rotating at the repetition rate of the comb) will measure maximal (anti)-squeezing. In the case of detuned squeezing,  $U(\omega)$  is complex and a stationary local oscillator will not necessarily measure maximal squeezing.

However, when measuring a symmetric double peak configuration one may obtain maximal squeezing [51]: when a local oscillator is equidistant between a nondegenerate squeezed state, measurement at the sideband frequency probes both modes. If the double peak is symmetric, we are summing two peaks with opposite Fourier components. Of course, as shown in Figure 3.(f-l) the double peak quadrature variance spectrum can be asymmetric.

#### 4.5 Additional data on LLE simulation

In order to support the theoretical conclusions and experimental observations, we preformed LLE simulations of a 2-FSR Kerr comb. The LLE simulates the classical comb dynamics [46], and allows us to focus on specific aspects, some not previously addressed in the experiment. Particularly, the squeezing structures, both detuned and non-detuned, significantly influence the formation of secondary combs. Hence, studying the primary comb to secondary comb transitions in a classical framework is valuable in the context of the findings presented in this work.

We start by simulating a perturbed dispersion yielding a comb similar to that of our experiment. The dispersion perturbation in our setup changes in response to heating. For the same reason, the perturbation also changes as a function of power in the cavity (i.e it is changing during the evolution of the comb). However, since the effects we describe do not require this behavior, we can observe the main features under constant dispersion. We use experimentally extracted parameters of  $D_2/2\pi = 1.2\text{MHz}$  and extract the perturbation parameters from the measured dispersion. For simplicity, we only use the perturbed modes near the pump modes  $-2, -1, 0, 1, 2$ . For quality factors, we use a constant value of 1.83 million, which we reduce at modes distant 17 FSR away from the pump to avoid pair generation there. The normalized pump power is  $f = 5.93$  where  $f^2 = 8g_0\kappa_c P_{in}/\kappa^3\hbar\omega_0$  and  $P_{in}$  is the input power,  $\kappa_c$  is the outcoupling power loss, and  $\omega_0$  is the pump angular frequency.

Importantly, the formation of our 2-FSR comb is not a direct result of the anomalous dispersion, but it is formed locally due to the dispersion defect (see Methods 4.3).

This means that the initial comb formation may be governed by adjusting the dispersion of sites  $-2, 0, 2$ . The detuning value of the threshold to a 1-FSR comb depends on the dispersion of the odd modes and the perturbation of modes  $-1, 1$ . By adjusting these parameters, we are able to simulate a comb evolution that is qualitatively similar to what we observe in the experiment.

Figures 5(a-b) and 11(a) show the comb evolution in the simulation, which is similar to our experiment (Fig. 9). The process begins with a 2-FSR primary comb which transitions to a 1-FSR secondary comb. Figure 11 demonstrates the transitions from one rolling Turing pattern to another. Since this transition is un-detuned, the first 1-FSR comb is a single phase locked comb and does not have sub combs.

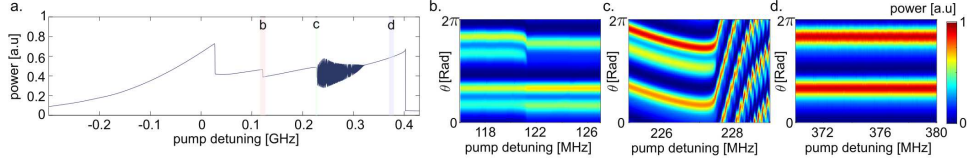


**Fig. 11 Intracavity field in real space for different regimes in the comb formation - LLE with perturbed dispersion - undetuned threshold.** **a.** Transmission as a function of continuous pump detuning (toward longer wavelengths). This plot is the same as in Fig. 5(a) but the shaded areas mark different regimes plotted in (b-d). **b.** Intracavity field in real space for the transition between the primary comb (2-FSR) and the secondary comb (1-FSR) corresponding to the shaded red region in a. **c.** Same as b but for the transition from the secondary comb (1-FSR) to a second detuned 1-FSR comb which oscillates (shaded green region). **d.** The region of a 2-FSR soliton crystal (shaded blue region).

The next transition involves the threshold crossing of a detuned 1-FSR comb, which produces an rf beatnote with the existing 1-FSR comb. The oscillations in this state are evident in both the transmission and the intra-cavity field (Fig. 11(c)). Finally the system transitions to a 2-FSR soliton crystal (Fig. 11(d)). To better understand the unique symmetric transition from a 2-FSR comb to a single phase locked 1-FSR comb, we explore the comb state at a pump detuning close to this threshold at 0.115 GHz. Figure 12(a-b) shows the comb from Fig. 11 for the detuning of 0.115 GHz in both the frequency (mode) space and real physical space respectively. Using the obtained comb amplitudes and the hot-cavity dispersion, we calculate the  $g^{(2)}$  correlations of each cavity-mode  $\mu$  with each cavity-mode  $\nu$ , which resembles the experimental  $g^{(2)}$  in Fig. 3(b). Next, we calculate the quadrature Hamiltonian  $M$  associated with the 2-FSR comb at 0.115GHz. The eigenspectrum is plotted in Fig. 12(d), showing that the non-detuned state (purely real eigenvalue) is approaching threshold. Correspondingly, the squeezing structure is a single peak (Fig. 12(e)), localized near the pump (Fig. 12(f)).

In addition to the perturbed dispersion case, we wish to explore in simulation the case of un-perturbed dispersion with a  $D_2 > 0$  term. Throughout this work, a perturbation in dispersion somewhat detached the general dispersion of the cavity from the frequency spacing of the 2-FSR Kerr comb, allowing for more possible behaviors. However, when a comb is formed without perturbation, the general dispersion and the comb's frequency spacing are more inherently linked, reducing the number of possible outcomes. While this case is conceptually simpler than the perturbed dispersion case, it

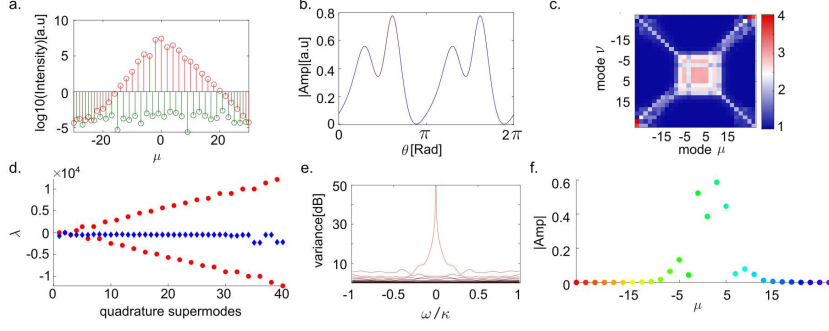


**Fig. 12 Examination of the simulated threshold between an un-detuned 2-FSR comb to an un-detuned 1-FSR comb at 0.115 GHz detuning.** **a.** Spectrum of the 2-FSR primary Kerr comb (red) and light in odd modes (green). **b.** Intracavity field in real space (rolling turing) **c.**  $g^{(2)}$  correlations of the below threshold light. **d.** Eigen-spectrum of the comb showing that an un-detuned supermode crosses threshold, and that the spectrum corresponds to the partially symmetric case. **e.** The squeezing structure, showing the single peak which correspond with the un-detuned supermode that crosses threshold in d. **f.** The spectrum of the most squeezed state

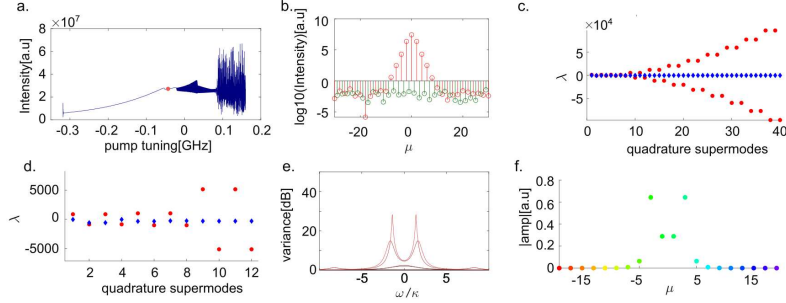


**Fig. 13 Simulation of a 2-FSR primary comb transition to a 1-FSR secondary comb in a unperturbed dispersion.** **a.** Transmission vs pump-detuning of the 2-FSR comb without dispersion perturbation. **b.** Spectrum of the 2-FSR Kerr comb (red) in an unperturbed dispersion. **c.** Eigen-spectrum showing 40 supermodes. In this case all the modes are detuned (purely imaginary eigenvalues) while the Hamiltonian is symmetric. **d.** Zoom-in on the spectrum in c. **e.** The squeezing structure, showing the double peak which correspond with the detuned state that crosses threshold in c,d **f.** The spectrum of the most squeezed state

can be more challenging to realize due to the high anomalous dispersion that is required for the 2-FSR comb to form (together with a relatively small FSR). Additionally, high anomalous dispersion causes the squeezed supermodes to localize in four modes, reducing the relevance of the lattice model description (Fig. 6). Nevertheless, this case does highlight some aspects which are relevant to the main case studied in this work. To generate a 2-FSR comb, we use high anomalous dispersion of  $D_2/2\pi = 86.4 \text{ MHz}$ , an intrinsic  $Q$  of 3.66 million and coupling  $Q$  of 4.25 million. These parameters result in a 2-FSR primary comb, which we pump at 12.55mW with CW light at 1545nm. This comb reaches threshold at a pump detuning of  $-0.04 \text{ GHz}$  (Fig. 13(a)). At this pump detuning value, even though the dispersion is symmetric and  $D'_1 = 0$ , the threshold

is still detuned (double peak). The symmetry implies that the eigenvalues are purely real or purely imaginary. Thus, if all the states are purely imaginary, there are no undetuned states in existence, leading to a double peak threshold. Correspondingly, the 2-FSR comb in Fig. 13b, for the detuning marked by the orange dot in Fig. 13(a), has a fully detuned spectrum (Fig. 13(c,d)). Such a spectrum is associated with a detuned threshold, *i.e.*, a squeezing spectrum that peaks away from zero. The localization that high  $D_2$  dispersion causes can be seen in the spectrum of the supermode in Fig. 13(f). The localization occurs for all supermodes, as Bragg scattering is not efficient away from the center of the comb.

**Acknowledgements.** We gratefully acknowledge discussions with Edwin Ng, Ryotatsu Yanagimoto, and Kiyoul Yang. This work is funded by the Defense Advanced Research Projects Agency under the QuICC program and by the NSF QuSeC-TAQS Award ID 2326792, as well as the Vannevar Bush Faculty Fellowship from the US Department of Defense. E.L acknowledges the Yad Hanadiv Rothschild fellowship, and the Zuckerman institute Zuckerman fellowship. Part of this work was performed at the Stanford Nanofabrication Facility (SNF) and the Stanford Nano Shared Facilities (SNSF). S. F. acknowledge the support of a MURI project for the U. S. Air Force Office of Scientific Research (Grant No. FA9550-22-1-0339). We thank NGK Insulators, Ltd. for 4H-SiCOI substrates used to fabricate devices in this work.

## References

- [1] McDonald, A., Pereg-Barnea, T., Clerk, A.A.: Phase-Dependent Chiral Transport and Effective Non-Hermitian Dynamics in a Bosonic Kitaev-Majorana Chain. *Physical Review X* **8**(4), 041031 (2018) <https://doi.org/10.1103/PhysRevX.8.041031>
- [2] Pino, J., Slim, J.J., Verhagen, E.: Non-Hermitian chiral phononics through optomechanically induced squeezing. *Nature* **606**(7912), 82–87 (2022) <https://doi.org/10.1038/s41586-022-04609-0>
- [3] Slim, J.J., Wanjura, C.C., Brunelli, M., Pino, J., Nunnenkamp, A., Verhagen, E.: Optomechanical realization of the bosonic Kitaev chain. *Nature* **627**(8005), 767–771 (2024) <https://doi.org/10.1038/s41586-024-07174-w>
- [4] Wan, L.-L., Lü, X.-Y.: Quantum-Squeezing-Induced Point-Gap Topology and Skin Effect. *Physical Review Letters* **130**(20), 203605 (2023) <https://doi.org/10.1103/PhysRevLett.130.203605>
- [5] Chembo, Y.K.: Quantum dynamics of Kerr optical frequency combs below and above threshold: Spontaneous four-wave mixing, entanglement, and squeezed states of light. *Physical Review A* **93**(3), 033820 (2016) <https://doi.org/10.1103/PhysRevA.93.033820>
- [6] Roy, A., Jahani, S., Langrock, C., Fejer, M., Marandi, A.: Spectral phase transitions in optical parametric oscillators. *Nature Communications* **12**(1), 835 (2021)



<https://doi.org/10.1038/s41467-021-21048-z>

- [7] Guidry, M.A., Lukin, D.M., Yang, K.Y., Trivedi, R., Vučković, J.: Quantum optics of soliton microcombs. *Nature Photonics* **16**(1), 52–58 (2022) <https://doi.org/10.1038/s41566-021-00901-z>
- [8] Javid, U.A., Lopez-Rios, R., Ling, J., Graf, A., Staffa, J., Lin, Q.: Chip-scale simulations in a quantum-correlated synthetic space. *Nature Photonics* **17**(10), 883–890 (2023) <https://doi.org/10.1038/s41566-023-01236-7>
- [9] Jahanbozorgi, M., Yang, Z., Sun, S., Chen, H., Liu, R., Wang, B., Yi, X.: Generation of squeezed quantum microcombs with silicon nitride integrated photonic circuits. *Optica* **10**(8), 1100–1101 (2023) <https://doi.org/10.1364/OPTICA.498670>
- [10] Roslund, J., Araújo, R.M., Jiang, S., Fabre, C., Treps, N.: Wavelength-multiplexed quantum networks with ultrafast frequency combs. *Nature Photonics* **8**(2), 109–112 (2014) <https://doi.org/10.1038/nphoton.2013.340>
- [11] Chen, M., Menicucci, N.C., Pfister, O.: Experimental realization of multipartite entanglement of 60 modes of a quantum optical frequency comb. *Physical review letters* **112**(12), 120505 (2014) <https://doi.org/10.1103/PhysRevLett.112.120505>
- [12] Cai, Y., Roslund, J., Ferrini, G., Arzani, F., Xu, X., Fabre, C., Treps, N.: Multimode entanglement in reconfigurable graph states using optical frequency combs. *Nature Communications* **8**(1), 15645 (2017) <https://doi.org/10.1038/ncomms15645>
- [13] Del’Haye, P., Schliesser, A., Arcizet, O., Wilken, T., Holzwarth, R., Kippenberg, T.J.: Optical frequency comb generation from a monolithic microresonator. *Nature* **450**(7173), 1214–1217 (2007) <https://doi.org/10.1038/nature06401>
- [14] Braunstein, S.L., Loock, P.: Quantum information with continuous variables. *Rev. Mod. Phys.* **77**, 513–577 (2005) <https://doi.org/10.1103/RevModPhys.77.513>
- [15] Rüter, C.E., Makris, K.G., El-Ganainy, R., Christodoulides, D.N., Segev, M., Kip, D.: Observation of parity–time symmetry in optics. *Nature Physics* **6**(3), 192–195 (2010) <https://doi.org/10.1038/nphys1515>
- [16] Wang, Y.-X., Clerk, A.A.: Non-Hermitian dynamics without dissipation in quantum systems. *Physical Review A* **99**(6), 063834 (2019) <https://doi.org/10.1103/PhysRevA.99.063834>
- [17] Flynn, V.P., Cobanera, E., Viola, L.: Deconstructing effective non-Hermitian dynamics in quadratic bosonic Hamiltonians. *New Journal of Physics* **22**(8), 083004 (2020) <https://doi.org/10.1088/1367-2630/ab9e87>

- [18] Wanjura, C.C., Slim, J.J., Pino, J., Brunelli, M., Verhagen, E., Nunnenkamp, A.: Quadrature nonreciprocity in bosonic networks without breaking time-reversal symmetry. *Nature Physics* **19**(10), 1429–1436 (2023) <https://doi.org/10.1038/s41567-023-02128-x>
- [19] Dutt, A., Minkov, M., Lin, Q., Yuan, L., Miller, D.A.B., Fan, S.: Experimental band structure spectroscopy along a synthetic dimension. *Nature Communications* **10**(1), 3122 (2019) <https://doi.org/10.1038/s41467-019-11117-9>
- [20] Dutt, A., Yuan, L., Yang, K.Y., Wang, K., Buddhiraju, S., Vučković, J., Fan, S.: Creating boundaries along a synthetic frequency dimension. *Nature Communications* **13**(1), 3377 (2022) <https://doi.org/10.1038/s41467-022-31140-7>
- [21] Wang, K., Dutt, A., Yang, K.Y., Wojcik, C.C., Vučković, J., Fan, S.: Generating arbitrary topological windings of a non-Hermitian band. *Science* **371**(6535), 1240–1245 (2021) <https://doi.org/10.1126/science.abf6568>
- [22] Leefmans, C.R., Englebert, N., Williams, J., Gray, R.M., Goldman, N., Gorza, S.-P., Leo, F., Marandi, A.: Cavity Soliton-Induced Topological Edge States. *arXiv* (2023). <https://doi.org/10.48550/arXiv.2311.04873>
- [23] Valcárcel, G.J., Patera, G., Treps, N., Fabre, C.: Multimode squeezing of frequency combs. *Physical Review A* **74**(6), 061801 (2006) <https://doi.org/10.1103/PhysRevA.74.061801>
- [24] Uddin, S.Z., Rivera, N., Seyler, D., Salamin, Y., Sloan, J., Roques-Carmes, C., Xu, S., Sander, M., Soljacic, M.: Quantum sensitivity analysis: a general framework for controlling quantum fluctuations. *arXiv* (2024). <http://arxiv.org/abs/2311.05535>
- [25] Herr, T., Brasch, V., Jost, J.D., Wang, C.Y., Kondratiev, N.M., Gorodetsky, M.L., Kippenberg, T.J.: Temporal solitons in optical microresonators. *Nature Photonics* **8**(2), 145–152 (2014) <https://doi.org/10.1038/nphoton.2013.343>
- [26] Cole, D.C., Lamb, E.S., Del’Haye, P., Diddams, S.A., Papp, S.B.: Soliton crystals in Kerr resonators. *Nature Photonics* **11**(10), 671–676 (2017) <https://doi.org/10.1038/s41566-017-0009-z>
- [27] Reimer, C., Kues, M., Roztock, P., Wetzel, B., Grazioso, F., Little, B.E., Chu, S.T., Johnston, T., Bromberg, Y., Caspani, L., Moss, D.J., Morandotti, R.: Generation of multiphoton entangled quantum states by means of integrated frequency combs. *Science* **351**(6278), 1176–1180 (2016) <https://doi.org/10.1126/science.aad8532>
- [28] Kues, M., Reimer, C., Roztock, P., Cortés, L.R., Sciara, S., Wetzel, B., Zhang, Y., Cino, A., Chu, S.T., Little, B.E., Moss, D.J., Caspani, L., Azaña, J., Morandotti, R.: On-chip generation of high-dimensional entangled quantum states and their coherent control. *Nature* **546**(7660), 622–626 (2017)

<https://doi.org/10.1038/nature22986>

- [29] Zhao, Y., Okawachi, Y., Jang, J.K., Ji, X., Lipson, M., Gaeta, A.L.: Near-degenerate quadrature-squeezed vacuum generation on a silicon-nitride chip. *Physical Review Letters* **124**(19), 193601 (2020) <https://doi.org/10.1103/PhysRevLett.124.193601>
- [30] Moille, G., Menyuk, C., Chembo, Y.K., Dutt, A., Srinivasan, K.: Synthetic Frequency Lattices from an Integrated Dispersive Multi-Color Soliton. *arXiv* (2022). <https://doi.org/10.48550/arXiv.2210.09036>
- [31] Englebert, N., Goldman, N., Erkintalo, M., Mostaan, N., Gorza, S.-P., Leo, F., Fatome, J.: Bloch oscillations of coherently driven dissipative solitons in a synthetic dimension. *Nature Physics* **19**(7), 1014–1021 (2023) <https://doi.org/10.1038/s41567-023-02005-7>
- [32] Bensemoun, A., Gonzalez-Arciniegas, C., Pfister, O., Labonté, L., Etesse, J., Martin, A., Tanzilli, S., Patera, G., d’Auria, V.: Multipartite entanglement in bright frequency combs out of microresonators. *Physics Letters A* **493**, 129272 (2024)
- [33] Guidry, M.A., Lukin, D.M., Yang, K.Y., Vučković, J.: Multimode squeezing in soliton crystal microcombs. *Optica* **10**(6), 694–701 (2023) <https://doi.org/10.1364/OPTICA.485996>
- [34] Gouzien, E., Labonte, L., Etesse, J., Zavatta, A., Tanzilli, S., D’Auria, V., Patera, G.: Hidden and detectable squeezing from microresonators. *Physical Review Research* **5**(2), 023178 (2023) <https://doi.org/10.1103/PhysRevResearch.5.023178>
- [35] Regensburger, A., Bersch, C., Miri, M.-A., Onishchukov, G., Christodoulides, D.N., Peschel, U.: Parity–time synthetic photonic lattices. *Nature* **488**(7410), 167–171 (2012) <https://doi.org/10.1038/nature11298>
- [36] Zeuner, J.M., Rechtsman, M.C., Plotnik, Y., Lumer, Y., Nolte, S., Rudner, M.S., Segev, M., Szameit, A.: Observation of a Topological Transition in the Bulk of a Non-Hermitian System. *Physical Review Letters* **115**(4), 040402 (2015) <https://doi.org/10.1103/PhysRevLett.115.040402>
- [37] Weimann, S., Kremer, M., Plotnik, Y., Lumer, Y., Nolte, S., Makris, K.G., Segev, M., Rechtsman, M.C., Szameit, A.: Topologically protected bound states in photonic parity–time-symmetric crystals. *Nature Materials* **16**(4), 433–438 (2017) <https://doi.org/10.1038/nmat4811>
- [38] Moille, G., Leonhardt, M., Paligora, D., Englebert, N., Leo, F., Fatome, J., Srinivasan, K., Erkintalo, M.: Parametrically driven pure-Kerr temporal solitons in a chip-integrated microcavity. *Nature Photonics* **18**(6), 617–624

- (2024) <https://doi.org/10.1038/s41566-024-01401-6> . Publisher: Nature Publishing Group. Accessed 2024-11-25
- [39] Coen, S., Haelterman, M.: Continuous-wave ultrahigh-repetition-rate pulse-train generation through modulational instability in a passive fiber cavity. *Optics Letters* **26**(1), 39–41 (2001) <https://doi.org/10.1364/OL.26.000039>
  - [40] Poli, C., Bellec, M., Kuhl, U., Mortessagne, F., Schomerus, H.: Selective enhancement of topologically induced interface states in a dielectric resonator chain. *Nature Communications* **6**(1), 6710 (2015) <https://doi.org/10.1038/ncomms7710>
  - [41] Luo, X.-W., Zhang, C., Du, S.: Quantum Squeezing and Sensing with Pseudo-Anti-Parity-Time Symmetry. *Physical Review Letters* **128**(17), 173602 (2022) <https://doi.org/10.1103/PhysRevLett.128.173602>
  - [42] McCuller, L., Whittle, C., Ganapathy, D., Komori, K., Tse, M., Fernandez-Galiana, A., Barsotti, L., Fritschel, P., MacInnis, M., Matichard, F., Mason, K., Mavalvala, N., Mittleman, R., Yu, H., Zucker, M.E., Evans, M.: Frequency-dependent squeezing for advanced ligo. *Phys. Rev. Lett.* **124**, 171102 (2020) <https://doi.org/10.1103/PhysRevLett.124.171102>
  - [43] Vahala, K.J.: Optical microcavities. *Nature* **424**(6950), 839–846 (2003) <https://doi.org/10.1038/nature01939>
  - [44] Lukin, D.M., Dory, C., Guidry, M.A., Yang, K.Y., Mishra, S.D., Trivedi, R., Radulaski, M., Sun, S., Vercruysse, D., Ahn, G.H., Vučković, J.: 4H-silicon-carbide-on-insulator for integrated quantum and nonlinear photonics. *Nature Photonics* **14**(5), 330–334 (2020) <https://doi.org/10.1038/s41566-019-0556-6>
  - [45] Herr, T., Hartinger, K., Riemensberger, J., Wang, C.Y., Gavartin, E., Holzwarth, R., Gorodetsky, M.L., Kippenberg, T.J.: Universal formation dynamics and noise of Kerr-frequency combs in microresonators. *Nature Photonics* **6**(7), 480–487 (2012) <https://doi.org/10.1038/nphoton.2012.127>
  - [46] Chembo, Y.K., Menyuk, C.R.: Spatiotemporal Lugiato-Lefever formalism for Kerr-comb generation in whispering-gallery-mode resonators. *Physical Review A* **87**(5), 053852 (2013) <https://doi.org/10.1103/PhysRevA.87.053852>
  - [47] Flower, C.J., Jalali Mehrabad, M., Xu, L., Moille, G., Suarez-Forero, D.G., Örsel, O., Bahl, G., Chembo, Y., Srinivasan, K., Mittal, S., Hafezi, M.: Observation of topological frequency combs. *Science* **384**(6702), 1356–1361 (2024) <https://doi.org/10.1126/science.ado0053> . Publisher: American Association for the Advancement of Science. Accessed 2024-09-26
  - [48] Gouzien, E., Tanzilli, S., D’Auria, V., Patera, G.: Morphing Supermodes: A Full Characterization for Enabling Multimode Quantum Optics. *Physical Review Letters* **125**(10), 103601 (2020) <https://doi.org/10.1103/PhysRevLett.125.103601>

- [49] Lustig, E., Weimann, S., Plotnik, Y., Lumer, Y., Bandres, M.A., Szameit, A., Segev, M.: Photonic topological insulator in synthetic dimensions. *Nature* **567**(7748), 356–360 (2019) <https://doi.org/10.1038/s41586-019-0943-7>
- [50] Yang, Z., Jahanbozorgi, M., Jeong, D., Sun, S., Pfister, O., Lee, H., Yi, X.: A squeezed quantum microcomb on a chip. *Nature Communications* **12**(1), 4781 (2021) <https://doi.org/10.1038/s41467-021-25054-z>
- [51] Marino, A.M., Stroud, J., Wong, V., Bennink, R.S., Boyd, R.W.: Bichromatic Local Oscillator for Detection of Two-Mode Squeezed States of Light. *Journal of the Optical Society of America B* **24**(2), 335 (2007) <https://doi.org/10.1364/JOSAB.24.000335>